Updated 2011 (see the various sections for authors).

32. PARTICLE DETECTORS FOR NON-ACCELERATOR PHYSICS

32.1. Introduction

Non-accelerator experiments have become increasingly important in particle physics. These include classical cosmic ray experiments, neutrino oscillation measurements, and searches for double-beta decay, dark matter candidates, and magnetic monopoles. The experimental methods are sometimes those familiar at accelerators (plastic scintillators, drift chambers, TRD's, *etc.*) but there is also instrumentation either not found at accelerators or applied in a radically different way. Examples are atmospheric scintillation detectors (Fly's Eye), massive Cherenkov detectors (Super-Kamiokande, IceCube), ultracold solid state detectors (CDMS). And, except for the cosmic ray detectors, radiologically ultra-pure materials are required.

In this section, some more important detectors special to terrestrial non-accelerator experiments are discussed. Techniques used in both accelerator and non-accelerator experiments are described in Sec. 28, Particle Detectors at Accelerators, some of which have been modified to accommodate the non-accelerator nuances.

Space-based detectors also use some unique instrumentation, but these are beyond the present scope of RPP.

32.2. High-energy cosmic-ray hadron and gamma-ray detectors

32.2.1. *Atmospheric fluorescence detectors* :
Updated August 2011 by L.R. Wiencke (Colorado School of Mines).

Cosmic-ray fluorescence detectors (FD) use the atmosphere as a giant calorimeter to measure isotropic scintillation light that traces the development profiles of extensive air showers (EAS). The EASs observed are produced by the interactions of high-energy ($E > 10^{17}$ eV) subatomic particles in the stratosphere and upper troposphere. The amount of scintillation light generated is proportional to energy deposited in the atmosphere and nearly independent of the primary species. Experiments with FDs include the pioneering Fly's Eye [1], HiRes [2], the Telescope Array [3], and the Pierre Auger Observatory [4]. The proposed JEM-EUSO [5] FD would tilt down to sweep across a much larger area from space.

The scintillation light is emitted between 290 and 430 nm (Fig. 32.1), when relativistic charged particles, primarily electrons and positrons, excite nitrogen molecules in air, resulting in transitions of the 1P and 2P systems. Reviews and references for the pioneering and ongoing laboratory measurements of fluorescence yield, $Y(\lambda, P, T, u)$, including dependence on wavelength (λ), temperature (T), pressure (p), and humidity (u) may be found in Refs. 6 and 7.

An FD element (telescope) consists of a non-tracking spherical mirror (3.5–13 m^2 and less than astronomical quality), a close-packed "camera" of PMTs (for example, Hamamatsu R9508 or Photonis XP3062) near the focal plane, and flash ADC readout system with a pulse and track-finding trigger scheme [8]. Simple reflector optics

(12° × 16° degree field of view (FOV) on 256 PMTs) and Schmidt optics (30° × 30° FOV on 440 PMTs), including a correcting element, have been used. Segmented mirrors have been fabricated from slumped or slumped/polished glass with anodized aluminium coating and from chemically anodized $AlMgSiO_5$ affixed to shaped aluminum. A broadband UV filter (custom fabricated or Schott MUG-6) covers the camera face or much larger entrance aperture to reduce background light such as starlight, airglow, man-made light pollution, and airplane strobelights.
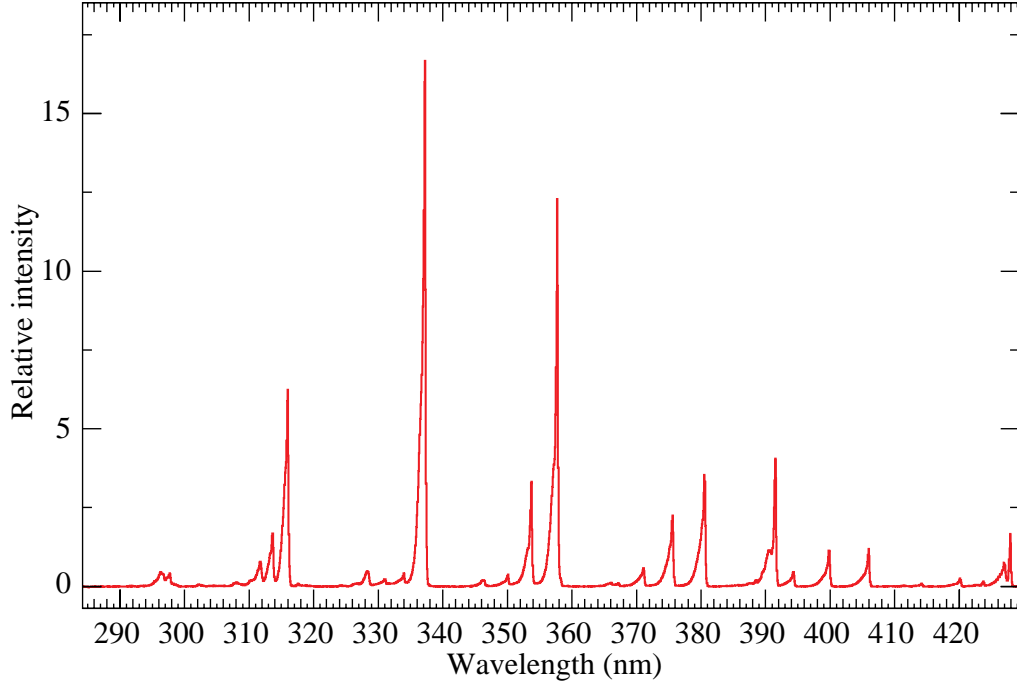

Figure 32.1: Measured fluorescence spectrum excited by 3 MeV electrons in dry air at 800 hPa and 293 K [9].

At 10^{20} eV, where the flux drops below 1 EAS/km²century, the aperture for an eye of adjacent FD telescopes that span the horizon can reach 10^4 km² sr. FD operation requires (nearly) moonless nights and clear atmospheric conditions, which imposes a duty cycle of about 10%. Arrangements of LEDs, calibrated diffuse sources [10], pulsed UV lasers [11], LIDARs* and cloud monitors are used for photometric calibration, atmospheric calibration [12], and determination of exposure [13].

The EAS generates a track consistent with a light source moving at $v = c$ across the FOV. The number of photons (N_γ) as a function of atmospheric depth (X) can be expressed as [7]

$$\frac{dN_\gamma}{dX} = \frac{dE_{\rm dep}^{\rm tot}}{dX} \int Y(\lambda, P, T, u) \cdot \tau_{\rm atm}(\lambda, X) \cdot \varepsilon_{\rm FD}(\lambda) d\lambda \quad , \tag{32.1}$$

---

* This acronym for "Light Detection and Ranging," refers here to systems that measure atmospheric properties from the light scattered backwards from laser pulses directed into the sky.

where $\tau_{atm}(\lambda, X)$ is atmospheric transmission, including wavelength (λ) dependence, and $\varepsilon_{\mathrm{FD}}(\lambda)$ is FD efficiency. $\varepsilon_{\mathrm{FD}}(\lambda)$ includes geometric factors and collection efficiency of the optics, quantum efficiency of the PMTs, and other throughput factors. The typical systematic uncertainties, Y (10–15%), τ_{atm} (10%) and $\varepsilon_{\mathrm{FD}}$ (photometric calibration 10%), currently dominate the total reconstructed EAS energy uncertainty. $\Delta E/E$ of 20–25% is possible, provided the geometric fit of the EAS axis is constrained by multi-eye stereo projection, or by timing from a colocated sparse array of surface detectors.

Analysis methods to reconstruct the EAS profile and deconvolute the contributions of re-scattered scintillation light, and direct and scattered Cherenkov light are described in [1] and more recently in [14]. The EAS energy is typically obtained by integrating over the Gaisser-Hillas function [15]

$$E_{\mathrm{cal}} = \int_0^\infty w_{\mathrm{max}} \left(\frac{X - X_0}{X_{\mathrm{max}} - X_0} \right)^{(X_{\mathrm{max}} - X_0)/\lambda} e^{(X_{\mathrm{max}} - X)/\lambda} \mathrm{d}X \quad , \qquad (32.2)$$

where X_{max} is the depth at which the shower reaches its maximum energy deposit w_{max}. X_0 and λ are two shape parameters.

32.2.2. *Atmospheric Cherenkov telescopes for high-energy γ-ray astronomy* : Written August 2009 by J. Holder (Bartol Research Inst., Univ. of Delaware).

A wide variety of astrophysical objects are now known to produce high-energy γ-ray photons. Leptonic or hadronic particle populations, accelerated to relativistic energies in the source, produce γ rays typically through inverse Compton boosting of ambient photons, or through the decay of neutral pions produced in hadronic interactions. At energies below $\sim$ 30 GeV, γ-ray emission can be detected directly using satellite or balloon-borne instrumentation, with an effective area approximately equal to the size of the detector (< 1 m^2). At higher energies, a technique with much larger effective collection area is required to measure astrophysical γ-ray fluxes, which decrease rapidly with increasing energy. Atmospheric Cherenkov detectors achieve effective collection areas of $\sim 10^5$ m^2 by employing the Earth's atmosphere as an intrinsic part of the detection technique.

As described in Chapter 26, a hadronic cosmic ray or high energy γ-ray incident on the Earth's atmosphere triggers a particle cascade, or air shower. Relativistic charged particles in the cascade produce Cherenkov radiation, which is emitted along the shower direction, resulting in a light pool on the ground with a radius of $\sim$ 130 m. Cherenkov light is produced throughout the cascade development, with the maximum emission occurring when the number of particles in the cascade is largest, at an altitude of $\sim$ 10 km for primary energies of 100 GeV–1 TeV. Following absorption and scattering in the atmosphere, the Cherenkov light at ground level peaks at a wavelength, $\lambda \approx 300$–350 nm. The photon density is typically $\sim$ 100 photons/m^2 at 1 TeV, arriving in a brief flash of a few nanoseconds duration. This Cherenkov pulse can be detected from any point within the light pool radius by using large reflecting surfaces to focus the Cherenkov light on to fast photon detectors (Fig. 32.2).

Modern atmospheric Cherenkov telescopes, such as those built and operated by the H.E.S.S. [17], MAGIC [18] and VERITAS [16] collaborations, consist of large (> 100 m^2)

segmented mirrors on steerable altitude-azimuth mounts. A camera, made from an array of up to 1000 photomultiplier tubes (PMTs) covering a field-of-view of up to 5.0° in diameter, is placed at the mirror focus and used to record a Cherenkov image of each air shower. Images are recorded at a rate of a few hundred Hz, the vast majority of which are due to showers with hadronic cosmic-ray primaries. The shape and orientation of the Cherenkov images are used to discriminate γ-ray photon events from this cosmic-ray background, and to reconstruct the photon energy and arrival direction. γ-ray images result from purely electromagnetic cascades and appear as narrow, elongated ellipses in the camera plane. The long axis of the ellipse corresponds to the vertical extension of the air shower, and points back towards the source position in the field-of-view. If multiple telescopes are used to view the same shower ("stereoscopy"), the source position is simply the intersection point of the various image axes. Cosmic-ray primaries produce secondaries with large transverse momenta, which initiate sub-showers. Their images are consequently wider and less regular than those with γ-ray primaries and, since the original charged particle has been deflected by galactic magnetic fields before reaching the Earth, the images have no preferred orientation.
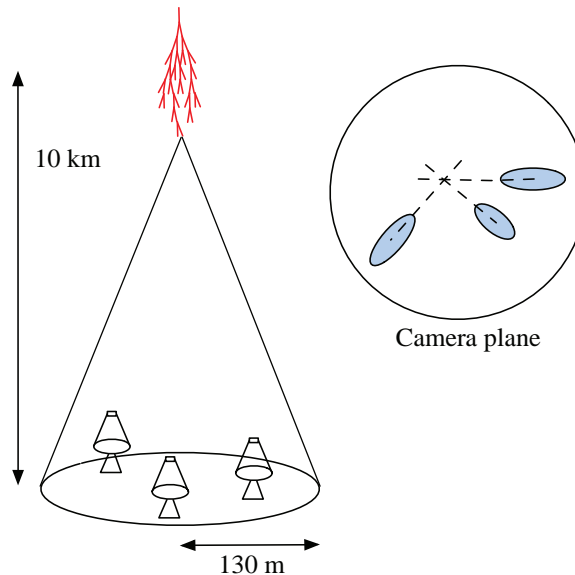
Figure 32.2: A schematic illustration of an atmospheric Cherenkov telescope array. The primary particle initiates an air shower, resulting in a cone of Cherenkov radiation. Telescopes within the Cherenkov light pool record elliptical images; the intersection of the long axes of these images indicates the arrival direction of the primary, and hence the location of a γ-ray source in the sky.

The measurable differences in Cherenkov image orientation and morphology provide the background discrimination which makes ground-based γ-ray astronomy possible. For point-like sources, such as distant Active Galactic Nuclei (AGNs), modern instruments can reject up to 99.999% of the triggered cosmic-ray events, while retaining up to 50% of the γ-ray population. In the case of spatially extended sources, such as Galactic supernova remnants (SNR), the background rejection is less efficient, but the technique

can be used to produce γ-ray maps of the emission from the source. The angular resolution depends upon the energy of the primary γ-ray, but is typically $0.1°$ per event (68% containment radius) at energies above a few hundred GeV.

The total Cherenkov yield from the air shower is proportional to the energy of the primary particle. The image intensity, combined with the reconstructed distance of the shower core from each telescope, can therefore be used to estimate the primary energy. The energy resolution of this technique, also energy-dependent, is typically 15–20% at energies above a few hundred GeV. Energy spectra of γ-ray sources can be measured over a wide range; potentially from ~ 50 GeV to ~ 100 TeV, depending upon the instrument characteristics, source strength, and exposure time. To a first approximation, the lower energy threshold at the trigger level, E_T, depends upon the mirror area, A, the photon collection efficiency, $\eta(\lambda)$, the Cherenkov light yield, $C(\lambda)$, the night sky background light, $B(\lambda)$, the solid angle, Ω, and the trigger resolving time, τ, as follows [19]:

$$E_T \propto \frac{1}{C(\lambda)} \sqrt{\frac{B(\lambda)\Omega\tau}{\eta(\lambda)A}} \tag{32.3}$$

In practice, this function may be modified by the properties of the detector; for example, by complex, multi-level, combinatorial trigger systems and highly pixellated fields of view. In addition, the useful scientific threshold, after the application of analysis cuts to select γ-ray events, is always somewhat higher than this.

The first astrophysical source to be convincingly detected using the imaging atmospheric Cherenkov technique was the Crab Nebula [20], with a flux of 2.1×10^{-11} photons $\text{cm}^{-2}\,\text{s}^{-1}$ above 1 TeV [21]. Modern arrays have sensitivity sufficient to detect sources with 1% of the Crab Nebula's flux in a few tens of hours, and the TeV source catalog now consists of more than 80 sources. The majority of these have been detected by scanning the Galactic plane from the southern hemisphere with the H.E.S.S. telescope array [22].

32.3. Large neutrino detectors

32.3.1. *Deep liquid detectors for rare processes* :
Revised November 2011 by K. Scholberg & C.W. Walter (Duke University)

Deep, large detectors for rare processes tend to be multi-purpose with physics reach that includes not only solar, reactor, supernova and atmospheric neutrinos, but also searches for baryon number violation, searches for exotic particles such as magnetic monopoles, and neutrino and cosmic ray astrophysics in different energy regimes. The detectors may also serve as targets for long-baseline neutrino beams for neutrino oscillation physics studies. In general, detector design considerations can be divided into high-and low-energy regimes, for which background and event reconstruction issues differ. The high-energy regime, from about 100 MeV to a few hundred GeV, is relevant for proton decay searches, atmospheric neutrinos and high-energy astrophysical neutrinos. The low-energy regime (a few tens of MeV or less) is relevant for supernova, solar, reactor and geological neutrinos.

Large water Cherenkov and scintillator detectors (see Table 32.1) usually consist of a volume of transparent liquid viewed by photomultiplier tubes (PMTs) (see Sec. 31.2);

Table 32.1: Properties of large detectors for rare processes. If total target mass is divided into large submodules, the number of subdetectors is indicated in parentheses.

Detector	Fid. mass, kton (modules)	PMTs (diameter, cm)	ξ	p.e./MeV	Dates
Baksan	0.33, scint (3150)	1/module (15)	segmented	40	1980–
MACRO	0.6, scint (476)	2-4/module (20)	segmented	18	1989–2000
LVD	1, scint. (840)	3/module (15)	segmented	15	1992–
KamLAND	1, scint	1325(43)+554(51)*	34%	460	2002–
Borexino	0.1, scint	2212 (20)	30%	500	2007–
SNO+	0.78, scint	9438 (20)	54%	400–900	Future
CHOOZ	0.005, scint (Gd)	192 (20)	15%	130	1997–1998
Double Chooz	0.020, scint (Gd)(2)	534/module (20)	13%	180	2011–
Daya Bay	0.160, scint (Gd)(8)	192/module (20)	5.6%[†]	100	2011–
RENO	0.030, scint (Gd)(2)	342/module (25)	12.6%	100	2011–
IMB-1	3.3, H_2O	2048 (12.5)	1%	0.25	1982–1985
IMB-2	3.3, H_2O	2048 (20)	4.5%	1.1	1987–1990
Kam I	0.88/0.78, H_2O	1000/948 (50)	20%	3.4	1983–1985
Kam II	1.04, H_2O	948 (50)	20%	3.4	1986–1990
Kam III	1.04, H_2O	948 (50)	20%[‡]	4.3	1990–1995
SK I	22.5, H_2O	11146 (50)	39%	6	1996–2001
SK II	22.5, H_2O	5182 (50)	19%	3	2002–2005
SK III+	22.5, H_2O	11129 (50)	39%	6	2006–
SNO	1, D_2O/1.7, H_2O	9438 (20)	31% [§]	9	1999–2006

* The 51 cm PMTs were added in 2003.
† The effective Daya Bay coverage is 12% with top and bottom reflectors.
‡ The effective Kamiokande III coverage was 25% with light collectors.
§ The effective SNO coverage was 54% with light collectors.

the liquid serves as active target. PMT hit charges and times are recorded and digitized, and triggering is usually based on coincidence of PMTs hits within a time window comparable to the detector's light-crossing time. Because photosensors lining an inner surface represent a driving cost that scales as surface area, very large volumes can be used for comparatively reasonable cost. Some detectors are segmented into subvolumes individually viewed by PMTs, and may include other detector elements (*e.g.*, tracking detectors). Devices to increase light collection, *e.g.*, reflectors or waveshifter plates, may be employed. A common configuration is to have at least one concentric outer layer

of liquid material separated from the inner part of the detector to serve as shielding against ambient background. If optically separated and instrumented with PMTs, an outer layer may also serve as an active veto against entering cosmic rays and other background events. The PMTs for large detectors typically range in size from 20 cm to 50 cm diameter, and typical quantum efficiencies are in the 20–25% range. The active liquid volume requires purification and there may be continuous recirculation of liquid. For large homogeneous detectors, the event interaction vertex is determined using relative timing of PMT hits, and energy deposition is determined from the number of recorded photoelectrons. A "fiducial volume" is usually defined within the full detector volume, some distance away from the PMT array. Inside the fiducial volume, enough PMTs are illuminated per event that reconstruction is considered reliable, and furthermore, entering background from the enclosing walls is suppressed by a buffer of self-shielding. PMT and detector optical parameters are calibrated using laser, LED, or other light sources. Quality of event reconstruction typically depends on photoelectron yield, pixelization and timing.

Because in most cases one is searching for rare events, large detectors are usually sited underground to reduce cosmic-ray related background (see Chapter 26). The minimum depth required varies according to the physics goals [23].

32.3.1.1. *Liquid scintillator detectors:*

Past and current large underground detectors based on hydrocarbon scintillators include LVD, MACRO, Baksan, Borexino, KamLAND and SNO+. Experiments at nuclear reactors include CHOOZ, Double CHOOZ, Daya Bay, and RENO. Organic liquid scintillators (see Sec. 31.3.0) for large detectors are chosen for high light yield and attenuation length, good stability, compatibility with other detector materials, high flash point, low toxicity, appropriate density for mechanical stability, and low cost. They may be doped with waveshifters and stabilizing agents. Popular choices are pseudocumene (1,2,4-trimethylbenzene) with a few g/L of the PPO (2,5-diphenyloxazole) fluor, and linear alkylbenzene (LAB). In a typical detector configuration there will be active or passive regions of undoped scintillator, non-scintillating mineral oil or water surrounding the inner neutrino target volume. A thin vessel or balloon made of nylon, acrylic or other material transparent to scintillation light may contain the inner target; if the scintillator is buoyant with respect to its buffer, ropes may hold the balloon in place. For phototube surface coverages in the 20–40% range, yields in the few hundreds of photoelectrons per MeV of energy deposition can be obtained. Typical energy resolution is about $7\%/\sqrt{E(\mathrm{MeV})}$, and typical position reconstruction resolution is a few tens of cm at ~ 1 MeV, scaling as $\sim N^{-1/2}$, where N is the number of photoelectrons detected.

Shallow detectors for reactor neutrino oscillation experiments require excellent muon veto capabilities. For $\bar{\nu}_e$ detection via inverse beta decay on free protons, $\bar{\nu}_e + p \rightarrow n + e^+$, the neutron is captured by a proton on a $\sim$180 μs timescale, resulting in a 2.2 MeV γ ray, observable by Compton scattering and which can be used as a tag in coincidence with the positron signal. The positron annihilation γ rays may also contribute. Inverse beta decay tagging may be improved by addition of Gd at $\sim$0.1% by mass, which for natural isotope abundance has a $\sim$49,000 barn cross-section for neutron capture (in contrast to the 0.3 barn cross-section for capture on free protons). Gd capture takes $\sim$30 μs, and

is followed by a cascade of γ rays adding up to about 8 MeV. Gadolinium doping of scintillator requires specialized formulation to ensure adequate attenuation length and stability.

Scintillation detectors have an advantage over water Cherenkov detectors in the lack of Cherenkov threshold and the high light yield. However, scintillation light emission is nearly isotropic, and therefore directional capabilities are relatively weak. Liquid scintillator is especially suitable for detection of low-energy events. Radioactive backgrounds are a serious issue, and include long-lived cosmogenics. To go below a few MeV, very careful selection of materials and purification of the scintillator is required (see Sec. 32.6). Fiducialization and tagging can reduce background. A recent idea, not yet realized, is to dissolve neutrinoless double beta decay ($0\nu\beta\beta$) isotopes in scintillator (for instance ^{150}Nd in SNO+). Although energy resolution is poor compared to typical $0\nu\beta\beta$ search experiments, the quantity of isotope could be so large that the kinematic signature of $0\nu\beta\beta$ would be visible as a clear feature in the spectrum.

32.3.1.2. *Water Cherenkov detectors:*

Very large-imaging water detectors reconstruct ten-meter-scale Cherenkov rings produced by charged particles (see Sec. 31.5.0). The first such large detectors were IMB and Kamiokande. The only currently existing instance of this class of detector, with fiducial volume of 22.5 kton and total mass of 50 kton, is Super-Kamiokande (Super-K). For volumes of this scale, absorption and scattering of Cherenkov light are non-negligible, and a wavelength-dependent factor $\exp(-d/L(\lambda))$ (where d is the distance from emission to the sensor and $L(\lambda)$ is the attenuation length of the medium) must be included in the integral of Eq. (31.5) for the photoelectron yield. Attenuation lengths on the order of 100 meters have been achieved.

Cherenkov detectors are excellent electromagnetic calorimeters, and the number of Cherenkov photons produced by an e/γ is nearly proportional to its kinetic energy. For massive particles, the number of photons produced is also related to the energy, but not linearly. For any type of particle, the *visible energy $E_{\rm vis}$* is defined as the energy of an electron which would produce the same number of Cherenkov photons. The number of collected photoelectrons depends on the scattering and attenuation in the water along with the photo-cathode coverage, quantum efficiency and the optical parameters of any external light collection systems or protective material surrounding them. Event-by-event corrections are made for geometry and attenuation. For a typical case, in water $N_{\rm p.e.} \sim 15\,\xi\,E_{\rm vis}({\rm MeV})$, where ξ is the effective fractional photosensor coverage. Cherenkov photoelectron yield per MeV of energy is relatively small compared to that for scintillator, *e.g.*, ~ 6 pe/MeV for Super-K with a PMT surface coverage of $\sim 40\%$. In spite of light yield and Cherenkov threshold issues, the intrinsic directionality of Cherenkov light allows individual particle tracks to be reconstructed. Vertex and direction fits are performed using PMT hit charges and times, requiring that the hit pattern be consistent with a Cherenkov ring.

High-energy ($\sim$100 MeV or more) neutrinos from the atmosphere or beams interact with nucleons; for the nucleons bound inside the ^{16}O nucleus, the nuclear effects both at the interaction, and as the particles leave the nucleus must be considered when reconstructing the interaction. Various event topologies can be distinguished by their

timing and fit patterns, and by presence or absence of light in a veto. "Fully-contained" events are those for which the neutrino interaction final state particles do not leave the inner part of the detector; these have their energies relatively well measured. Neutrino interactions for which the lepton is not contained in the inner detector sample have higher-energy parent neutrino energy distributions. For example, in "partially-contained" events, the neutrino interacts inside the inner part of the detector but the lepton (almost always a muon, since only muons are penetrating) exits. "Upward-going muons" can arise from neutrinos which interact in the rock below the detector and create muons which enter the detector and either stop, or go all the way through (entering downward-going muons cannot be distinguished from cosmic rays). At high energies, multi-photoelectron hits are likely and the charge collected by each PMT (rather than the number of PMTs firing) must be used; this degrades the energy resolution to approximately $2\%/\sqrt{\xi\, E_{\rm vis}({\rm GeV})}$. The absolute energy scale in this regime can be known to $\approx$2–3% using cosmic-ray muon energy deposition, Michel electrons and π^0 from atmospheric neutrino interactions. Typical vertex resolutions for GeV energies are a few tens of cm [24]. Angular resolution for determination of the direction of a charged particle track is a few degrees. For a neutrino interaction, because some final-state particles are usually below Cherenkov threshold, knowledge of direction of the incoming neutrino direction itself is generally worse than that of the lepton direction, and dependent on neutrino energy.

Multiple particles in an interaction (so long as they are above Cherenkov threshold) may be reconstructed, allowing for the exclusive reconstruction of final states. In searches for proton decay, multiple particles can be kinematically reconstructed to form a decaying nucleon. High-quality particle identification is also possible: γ rays and electrons shower, and electrons scatter, which results in fuzzy rings, whereas muons, pions and protons make sharp rings. These patterns can be quantitatively separated with high reliability using maximum likelihood methods [25]. A e/μ misidentification probability of $\sim 0.4\%/\xi$ in the sub-GeV range is consistent with the performance of several experiments for $4\% < \xi < 40\%$. Sources of background for high energy interactions include misidentified cosmic muons and anomalous light patterns when the PMTs sometimes "flash" and emit photons themselves. The latter class of events can be removed using its distinctive PMT signal patterns, which may be repeated. More information about high energy event selection and reconstruction may be found in reference [26].

In spite of the fairly low light yield, large water Cherenkov detectors may be employed for reconstructing low-energy events, down to *e.g.* $\sim$ 4-5 MeV for Super-K [27]. Low-energy neutrino interactions of solar neutrinos in water are predominantly elastic scattering off atomic electrons; single electron events are then reconstructed. At solar neutrino energies, the visible energy resolution ($\sim 30\%/\sqrt{\xi\, E_{\rm vis}({\rm MeV})}$) is about 20% worse than photoelectron counting statistics would imply. Using an electron LINAC and/or nuclear sources, 0.5–1.5% determination of the absolute energy scale has been achieved at solar neutrino energies. Angular resolution is limited by multiple scattering in this energy regime (25–30°). At these energies, radioactive backgrounds become a dominant issue. These backgrounds include radon in the water itself or emanated by detector materials, and γ rays from the rock and detector materials. In the few to few tens of MeV range, radioactive products of cosmic ray muon-induced spallation are

troublesome, and are removed by proximity in time and space to preceding muons, at some cost in dead time.

The Sudbury Neutrino Observatory (SNO) detector [28] is the only instance of a large heavy water detector and deserves mention here. In addition to an outer 1.7 kton of light water, SNO contained 1 kton of D_2O, giving it unique sensitivity to neutrino neutral current ($\nu_x + d \to \nu_x + p + n$), and charged current ($\nu_e + d \to p + p + e^-$) deuteron breakup reactions. The neutrons were detected in three ways: In the first phase, via the reaction $n + d \to t + \gamma + 6.25$ MeV; Cherenkov radiation from electrons Compton-scattered by the γ rays was observed. In the second phase, NaCl was dissolved in the water. ^{35}Cl captures neutrons, $n + {}^{35}Cl \to {}^{36}Cl + \gamma + 8.6$ MeV. The γ rays were observed via Compton scattering. In a final phase, specialized low-background ^3He counters ("neutral current detectors" or NCDs) were deployed in the detector. These detected neutrons via $n + {}^3He \to p + t + 0.76$ MeV, and ionization charge from energy loss of the products was recorded in proportional counters.

32.3.2. *Coherent radio Cherenkov radiation detectors* :
Written October 2011 by S.R. Klein (LBNL)

Radio detectors sensitive to coherent Cherenkov radiation provide an attractive way to search for ultra-high energy cosmic neutrinos. These neutrinos are the only long-range probe of the ultra-high energy cosmos. Protons and heavier nuclei with energies $\gtrsim 5 \times 10^{19}$ eV are limited to ranges of less than 100 Mpc by interactions with CMB photons (the GZK effect [29]) , and gamma rays pair-produce from the CMB. The decay products of the particles produced in the hadronic interactions include neutrinos. To detect a useful number of these "GZK neutrinos" annually (assuming that ultra-high energy cosmic rays are protons) requires a detector of about 100 km^3 in volume. This is too big for an optical Cherenkov detector. Optical attenuation lengths are less than 200 m in ice or water, so a 100 km^3 detector would require a prohibitive number of sensors.

Electromagnetic and hadronic showers produce radio pulses via the Askaryan effect [30], as discussed in Sec. 30. The shower contains more electrons than positrons, leading to coherent emission. The electric field strength is proportional to the neutrino energy; the radiated power goes as its square. Detectors with antennas placed in the active volume have thresholds around 10^{17} eV.

The electric field strength increases linearly with frequency, up to a cut-off wavelength set by the transverse size of the shower. The cut-off is about 1 GHz in ice, and 2.5 GHz in rock/lunar regolith. The broadband spectrum argues for a wide detection bandwidth, but, dispersion during signal transmission can cause technical challenges. The angular distribution depends on the frequency. Near the cutoff frequency, radiation is emitted in a narrow cone, centered around the Cherenov angle (about 56° in ice) [31]. At lower frequencies, the angular distribution broadens, eventually becoming largely isotropic. The signal is linearly polarized in the plane containing the shower direction and the photon direction. This polarization is a useful check that any observed signal is indeed coherent Cherenkov radiation. Polarization measurements can be used to help reconstruct the neutrino direction.

Radiodetection requires a dielectric medium, with a long absorption length for radio
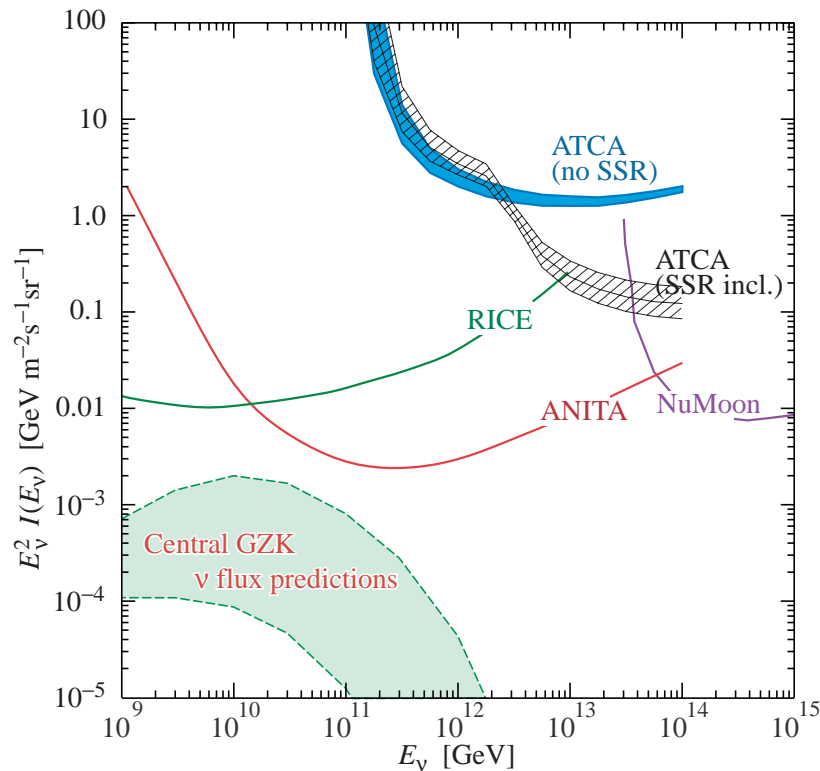
Figure 32.3: Representative ν flux limits from radio-detection experiments, illustrating the energy ranges for different techniques. Shown are limits from the Rice, ANITA, NuMoon and Lunaska (ATCA) collaborations. NuMoon and Lunaska are low and high frequency lunar scans respectively, showing the strengths of the two different frequency bands. The two separate limits for ATCA are for different models of the lunar regolith; their separation is a measure of the resultant uncertainty. Also shown, for comparison is the mid-range of flux predictions for GZK neutrinos from Ref. 34.

waves. The huge target volumes require that this be a commonly available natural material, usually Antarctic ice or the lunar regolith [32].

When viewed from near the Cherenkov angle, the experimental signal is a short wideband radio pulse coming from a shower-sized region within a solid. The initial pulse width is ≈ 1 ns, but it may be broadened by dispersion as it propagates. As long as the dispersion can be accounted for, a large bandwidth detector is the most sensitive. Because the angular distribution depends on the frequency, spectral information can be used to help reconstruct the neutrino direction.

Radio detectors have observed cosmic-ray air showers in the atmosphere. The physics of radio-wave generation in air showers is more complex because there are contributions due to charge separation by charged particles, and from synchrotron radiation from $e^{\pm}$, both due to the Earth's magnetic field. Several experiments have also set limits on radiation due to magnetic monopoles.

32.3.2.1. *The Moon as a target:*

Because of it's large size and non-conducting regolith, and the availability of large radio-telescopes, the moon is an attractive target [33]; several representative lunar experiments are listed in Table 32.2. Conventional radio-telescopes are reasonably well suited to lunar neutrino searches, with natural beam widths not too dissimilar from the size of the Moon. Still, there are some experimental challenges in understanding the signal. The composition of the lunar regolith is not well known, and the attenuation length for radio waves must be estimated. An attenuation length of 9/f(GHz) (m) is often used. The big limitation of lunar experiments is that the 240,000 km target-antenna separation leads to neutrino energy thresholds far above 10^{20} eV.

Table 32.2: Experiments that have set limits on neutrino interactions in the Moon; current limits are shown in Fig. 32.3 [32].

Experiment	Year	Dish Size	Frequency	Bandwidth	Obs. Time
Parkes	1995	64 m	1425 MHz	500 MHz	10 hrs
Glue	1999+	70 m, 34 m	2200 MHz	40-150 MHz	120 hrs
NuMoon	2008	11×25 m	115–180 MHz	—	50 hrs
Lunaska	2008	3× 22 m	1200–1800 MHz	—	6 nights
Resun	2008	4× 25 m	1450 MHz	50 MHz	45 hours

The frequency range affects the sensitive volume. At low frequencies, radiation is relatively isotropic, so signals can be detected from most of the Moon's surface, for most angles of incidence. At higher frequencies, the signal is stronger, but radiation is concentrated near the Cherenkov angle, and the geometry limits the sensitivity to interactions near the Moon's limb, where the neutrino also arrives within a fairly narrow angular range. The larger high-frequency attenuation limits the depth that can be probed.

So, higher frequency searches probe lower neutrino energies, but lower frequency searches can set tighter flux limits on high-energy neutrinos. An alternative approach, increasingly viable with modern technology, is to search over a wide frequency range. This introduces a technical challenge in the form of dispersion (frequency dependent time delays) in the ionosphere. The Parkes experiment pioneered the use of de-dispersion filters; this has been taken to a high art by the Lunaska collaboration.

Lunar experiments use several techniques to reject backgrounds, which are mostly anthropogenic. Many experiments use multiple antennas, separated by at least hundreds of meters; by requiring a coincidence within a small time window, anthropogenic noise can be rejected. An alternative approach is to use beam forming with multiple receivers in a single antenna, to ensure that the signal points back to the moon. The limits set by representative lunar experiments are shown in Fig. 32.3.

These efforts have considerable scope for expansion. In the near future, several large radio detector arrays should reach significantly lower limits. The LOFAR array is beginning to take data with 36 detector clusters spread over Northwest Europe. In the

longer term, the Square Kilometer Array (SKA) with 1 km^2 effective area will push thresholds down to near 10^{20} eV.

32.3.2.2. *The ANITA balloon experiment:*

To reduce the energy threshold, it is necessary to reduce the antenna-target separation. Most of these experiments use Antarctic ice as a medium. One such experiment is the ANITA balloon experiment which made two flights around Antarctica, floating at an altitude around 35 km [34]. Its 40 (32 in the first flight) dual-polarization horn antennas scanned the surrounding ice, out to the horizon (650 km away). Because of the small angle of incidence, ANITA was able to make use of polarization information; ν signals should be vertically polarized, while most background from cosmic-ray air showers is expected to be horizontally polarized. By using the several-meter separation between antennas, ANITA achieved a pointing accuracy of 0.2-0.4^0 in elevation, and 0.5-1.1^0 in azimuth.

Antarctic experiments must consider the inhomogeneities in the ice: varying density in the upper ice (the firn) and the variation in radio attenuation length with temperature. ANITA also had to consider the surface roughness, which affects the transition from ice to air. All of these affect the propagation of radio-waves from the ν-induced shower to the antennas.

The 'firn' is the top 100-200 m of Antarctic ice, where there is a transition from packed snow at the surface to solid ice (density 0.92 g/cm^3) below, where the density increases gradually with depth. The index of refraction depends on the density, so radio waves bend downward in the firn. This bending reduces the effectiveness of surface or aerial antennas. The thickness of the firn varies with location; it is thicker in central Antarctica than in the coastal ice sheets.

The attenuation length of radio waves depends on the frequency and ice temperature, with attenuation higher in warmer ice. A recent measurement, by the ARA collaboration at the South Pole found an average attenuation length of 670^{+180}_{-66} m [35]. On the Ross Ice Shelf, ARIANNA finds attenuation lengths of 300-500 m, depending on frequency [36].

ANITA verified the accuracy of their calibrations by observing radio sources that they buried in the ice. ANITA has also recently observed radio waves from cosmic-ray air showers; these showers are differentiated from neutrino showers on the basis of the radio polarization and zenith angle distribution [37].

As with the lunar experiments, ANITA had to contend with anthropogenic backgrounds. They used their good pointing accuracy to remove all candidate events that pointed toward known or suspected areas of human habitation. The limit from their two flights is shown in Fig. 32.3. These are the most stringent limits on GZK neutrinos to date. Because of the significant target to detector separation, ANITA is most sensitive at energies above 10^{19} eV, above the peak of the GZK neutrino spectrum.

32.3.2.3. *Active Volume Detectors:*

The use of radio antennas located in the active volume was pioneered by the RICE experiment, which buried radio antennas in holes drilled for AMANDA [38] at the South Pole. RICE was comprised of 18 half-wave dipole antennas, sensitive from 200 MHz to 1 GHz, buried between 100 and 300 m deep. Each antenna fed an in-situ preamplifier which transmitted the signals to surface digitizing electronics. The array triggered when four or more stations fired discriminators within 1.2 μs, giving it a threshold of about 10^{17} eV.

Two groups are prototyping detectors, with the goal of a detector with an active volume in the 100 km^3 range. Both techniques are modular, so the detector volume scales roughly linearly with the available funding. The Askaryan Radio Array (ARA) is located at the South Pole, while the Antarctic Ross Iceshelf ANtenna Neutrino Array (ARIANNA) is on the Ross Ice Shelf. Both experiments use local triggers based on a coincidence between multiple antennas in a single station/cluster.

One big difference between the two experiments is the depth of their antennas. ARA buries antennas up to 200 m deep in the ice, to avoid the firn. Because of the refraction, a surface antenna cannot 'see' a signal from a near-surface interaction some distance away. Burying antennas avoids this problem. However, drilling holes has costs, and the limited hole diameter (15 cm in ARA) requires compromises between antenna design (particularly for horizontally polarized waves), mechanical support, power and communications. In contrast, ARIANNA places antennas in shallow, near-surface holes. This greatly simplifies deployment and avoid limitations on antenna design, but at a cost of reduced sensitivity to neutrino interactions near the surface.

The current ARA proposal, ARA-37 [35], calls for an array of 37 stations, each consisting of 16 embedded antennas deployed up to 200 m deep below the firn) in several 15-cm diameter boreholes. ARA will detect signals in the frequency range from 150 to 850 MHz for vertical polarization, and 250 MHz to 850 MHz for horizontal polarization. ARA plans to use bicone antennas for vertical polarization, and quad-slotted cylinders for horizontal polarization. The collaboration uses notch filters and surface veto antennas to eliminate most anthropogenic noise, and vetos events when aircraft are in the area, or weather balloons are being launched.

ARIANNA will be located in Moore's Bay, on the Ross Ice Shelf, where $\approx 575\,\mathrm{m}$ of ice sits atop the Ross Sea [36]. The site was chosen because the ice-seawater interface is smooth there, so the interface acts as a mirror for radio waves. The major advantage of this approach is that ARIANNA is sensitive to downward going neutrinos, and should be able to see more of the Cherenkov cone for horizontal neutrinos. One disadvantage of the site is that the ice is warmer, so the radio attenuation length will be shorter. Each ARIANNA station will use 8 log-periodic dipole antennas, pointing downward and arranged in an octagon. The multiple antennas allow for single-station directional and polarization measurements. The ARIANNA site is about 110 km from McMurdo station, and is shielded by Minna Bluff.

32.4. Large time-projection chambers for rare event detection

Written August 2009 by M. Heffner (LLNL).

The Time Projection Chamber (TPC) concept (Sec. 31.6.5) has been applied to many projects outside of particle physics and the accelerator-based experiments for which it was initially developed. TPCs in non-accelerator particle physics experiments are principally focused on rare event detection (*e.g.*, neutrino and dark matter experiments) and the physics of these experiments can place dramatically different constraints on the TPC design (only extensions of the traditional TPCs are discussed here). The drift gas or liquid is usually the target or matter under observation and due to very low signal rates a TPC with the largest possible active mass is desired. The large mass complicates particle tracking of short and sometimes very low-energy particles. Other special design issues include efficient light collection, background rejection, internal triggering, and optimal energy resolution.

Backgrounds from γ rays and neutrons are significant design issues in the construction of these TPCs. These are generally placed deep underground to shield them from cosmogenic particles and are surrounded with shielding to reduce radiation from the local surroundings. The construction materials are carefully screened for radiopurity, as they are in close contact with the active mass and can be a significant source of background. The TPC excels in reducing this internal background because the mass inside the field cage forms one monolithic volume from which fiducial cuts can be made *ex post facto* to isolate quiet drift mass. The liquid (gas) can be circulated and purified to a very high level. Self-shielding in these large mass systems can be significant and the effect improves with density and size. (See Sec. 32.6.)

The liquid-phase TPC can have a high density at low pressure that results in very good self-shielding and compact installation with lightweight containment. The down sides are the need for cryogenics, slower charge drift, tracks shorter than typical electron diffusion distances, lower-energy resolution (*e.g.*, xenon) and limited charge readout options. Slower charge drift requires long electron lifetimes, placing strict limits on the oxygen and other impurities with high electron affinity. A significant variation of the liquid-phase TPC that improves the charge readout is the dual-phase TPC, where a gas phase layer is formed above the liquid into which the drifting electrons are extracted and amplified, typically with electroluminescence (*i.e.*, secondary scintillation or proportional scintillation (Fig. 32.4)). The successful transfer of electrons across the phase boundary requires careful control of its position and setting up an appropriate electric field.

A high-pressure gas phase TPC has no cryogenics and density is easily optimized for the signal, but a large heavy-pressure vessel is required. Although self shielding is reduced, it can in some cases approach that of the liquid phase; in xenon at 50 atm the density is about half that of water or about 1/6 of liquid xenon. A significant feature of high pressure xenon gas is the energy resolution. Below a density of about $0.5\,\mathrm{g\,cm^{-3}}$ the intrinsic resolution is only a few times that of high purity germanium [40]. A neutrinoless double beta decay ($0\nu2\beta$) search with a TPC operated below this density limit could enjoy excellent energy resolution and maintain particle tracking for background rejection.

An observable interaction with the TPC results in a charged particle that travels in the drift matter, exciting and ionizing the atoms until the initial energy is converted
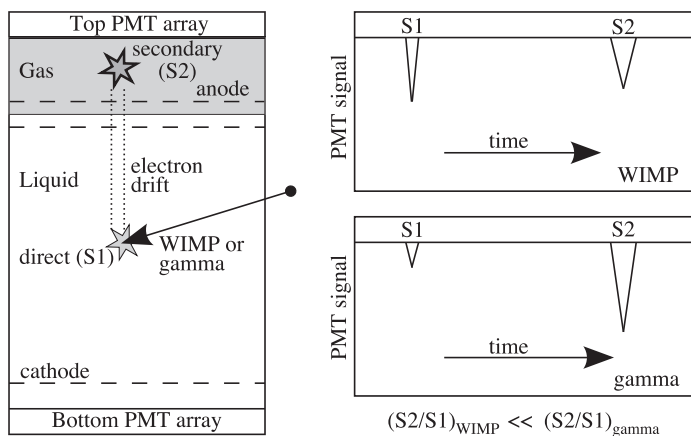
Figure 32.4: The configuration of a dual phase detector is shown on the left with the locations of where the primary and secondary light are generated. On the right is a schematic view of the signals of both an electron and nuclear interaction illustrating the discrimination power of this method. This figure is slightly modified from Ref. 39.

into ionization, scintillation, or heat with relatively large fluctuations around the mean. Rare-event TPCs can be designed to detect scintillation light as well as charge to exploit the anti-correlation to improve energy resolution and/or signal to noise [41]. An electric drift field separates the electrons and positive ions from the ionization although the separation is not complete and some electrons are captured, exciting atoms and releasing more light than the primary excitation alone. The average partition between the scintillation and ionization can be manipulated to increase the ionization (at the expense of scintillation) by a number of methods, such as increasing the strength of the electric field up to saturation of the ionization yield, increasing the temperature to enhance the diffusion of the ionized electrons, and adding dopants such as triethylamine that can be photoionized by the scintillation photons releasing more ionization.

Scintillation light is typically collected with photomultiplier tubes (PMTs) and avalanche photo diodes (APDs) although any fast (compared to the ionization drift speed) light collector capable of detecting the typically UV photons, maintaining high radiopurity, and perhaps withstanding pressure would work. (CCDs are slow and therefore only record two dimensions, integrating over the time direction. Some of the 3D information can be recovered by a few PMTs.) In most cases, coating the optics or adding a wavelength shifter is required [41], although some work has been done to directly readout the 175 nm light from xenon with a silicon detector. In a typical cylindrical geometry, the light detectors are placed at the ends on an equipotential of the field cage simplifying the design, but limiting the collection efficiency. The field cage can be made of UV-reflective materials such as Teflon, to increase the light-collection efficiency.

Charge collection can be accomplished with proportional avalanche in the manner used in a traditional TPC (even in the liquid state), although the final signal suffers from rather large fluctuations caused by small fluctuations early in the avalanche that are amplified by the process. Inductive readout of passing charges and direct collection of the unamplified charge do not rely on an avalanche, and are effective where energy

resolution is of paramount importance, but depend on low-noise amplifiers and relatively large signals (*e.g.*, in $0\nu 2\beta$ decay).

Electroluminescence can be used to proportionally amplify the the drifted ionization, and it does not suffer the fluctuations of an avalanche or the small signals of direct collection. It works by setting up at the positive end of the drift volume parallel meshes or wire arrays with an electric field larger than the drift field, but less than the field needed for avalanche. In xenon, this is 3–6 $\mathrm{kV\,cm^{-1}\,bar^{-1}}$ for good energy resolution. Eq. (32.4) shows the dependence of the yield (Y) in zenon in units of photons/(electron cm bar) as a function of pressure (p) in units of bar and electric field (E) in units of kV/cm [42]:

$$Y/p = 140\,E/p - 116 \ . \tag{32.4}$$

The amplification can be adjusted with the length of the electroluminescence region, pressure and electric field.
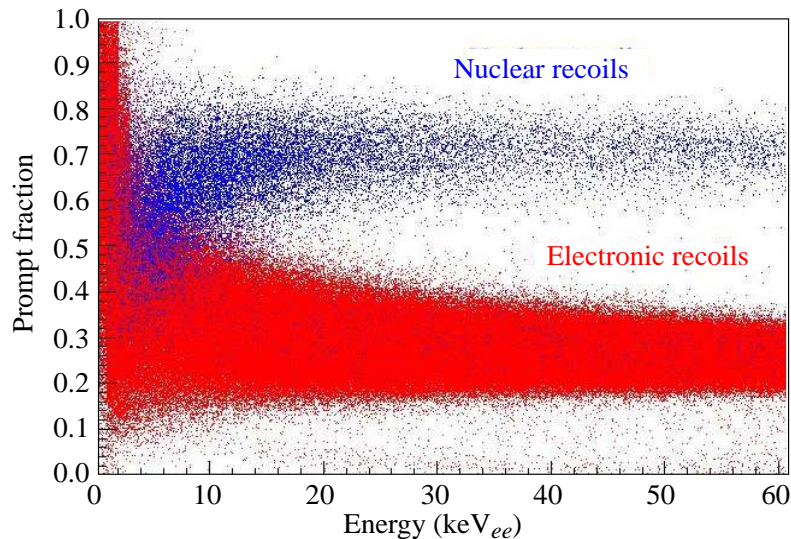

Figure 32.5: An example of pulse-shape discrimination of nuclear recoils and electrons in argon. The prompt fraction is a measure of the pulse shape that clearly separates the two interactions down to very low energy. Figure from Ref. 43.

Differentiation of nuclear and electron recoils at low-energy deposition is important as a means of background rejection. The nuclear recoil deposits a higher density of ionization than an electron recoil and this results in a higher geminate recombination resulting in a higher output of primary scintillation and lower charge. The ratio of scintillation to charge can be used to distinguish the two. In the case of an electroluminescence readout, this is done simply with the ratio of primary light to secondary light. Optically transparent grids with PMT or APD readout combine to make a elegant setup wherein the same array can measure the primary scintillation (S1), and the electroluminescence (S2) eliminating the necessity of two sets of readout detectors. Fig. 32.4 illustrates this method that works in the gas phase and in dual phase detectors. The time evolution of the primary light is also affected by the type of recoil that results from different

populations of excimers in the singlet and triplet states [43]. This alone has resulted in excellent discrimination, particularly in gasses where the decay times are significantly different (see Table 32.3). An example of the discrimination is displayed in Fig. 32.5, where nuclear recoils and electrons can be identified down to 10's of keV_{ee}, in argon. Nuclear recoils deposit less ionization than electrons at a given energy. For this reason, nuclear recoil energy is typically reported in equivalent electron energy loss, keV_{ee}, when compared with electrons.

The composition of the drift matter is an important choice in TPC design, and the noble gasses are frequently selected as the bulk element in the mix (Table 32.3). The noble gases have no electron affinity in the ground state, resulting in good free-electron lifetime and a good amount of scintillation that is useful for particle identification and t_0 determination. In the case of argon and xenon, the low average energy to produce an ion pair results in good energy resolution. The noble gases are easily purified to a high level that, combined with moderate cost, enables the construction of large monolithic detectors. Of the noble gasses one isotope of xenon (^{136}Xe) is a candidate for ($0\nu2\beta$).

Table 32.3: Properties of the noble gasses typically used in non-accelerator TPCs [44,45]. W is the average energy spent to produce one electron ion pair.

Element	W (eV)	photon yield (γ/keV)	wave-length (nm)	decay time (fast/slow)	cost* ($/kg)
Helium	46.0	50	80	$10\,\text{ns}/1.6\,\mu\text{s}$	$52
Neon	36.6	30	77	$10\,\text{ns}/3.9\,\mu\text{s}$	$330
Argon	26.4	40	128	$4\,\text{ns}/1.6\,\mu\text{s}$	$5
Xenon	21.7	42	175	$4\,\text{ns}/22\,\text{ns}$	$1200

* Prices from `chemcool.com` as updated in 2011.

The negative-ion TPC [46] uses an electronegative gas (*e.g.*, CS_2) either as the drift gas or as a dopant to the drift gas that captures the primary electrons, forming negative ions that drift in the electric field. Upon reaching the gas-gain region of the TPC, the electron is stripped from the ion in the high electric field, and the electron avalanches in the normal manner. The larger mass of the the negative ion keeps the kinetic energy of the ion thermal at high electric fields, and therefore such a TPC exhibits far less diffusion. The reduction of diffusion over large distance (time) enables detailed tracking of small tracks in a large volume without the benefit of a magnetic field to limit diffusion (which would be prohibitively expensive for a large volume). The trade-off is orders-of-magnitude slower drift, placing a limit on the trigger rate.

32.5. Sub-Kelvin detectors

Written September 2009 by S. Golwala (Caltech).

Detectors operating below 1 K, also known as "low-temperature" or "cryogenic" detectors, use $\lesssim$meV quanta (phonons, superconducting quasiparticles) to provide better energy resolution than is typically available from conventional technologies. Such resolution can provide unique advantages to applications reliant on energy resolution, such as beta-decay experiments seeking to measure the ν_e mass or searches for neutrinoless double-beta decay. In addition, the sub-Kelvin mode is combined with conventional (eV quanta) ionization or scintillation measurements to provide discrimination of nuclear recoils from electron recoils, critical for searches for WIMP dark matter and for coherent neutrino-nucleus scattering. We describe the techniques in generic fashion in the text and provide a list of experiments using these techniques in An excellent review [47] is available that covers this material and other applications of low-temperature detectors. The proceedings of the Low Temperature Detectors Workshops are also useful [48].

32.5.1. *Thermal Phonons* :

The most basic kind of low-temperature detector employs a dielectric absorber coupled to a thermal bath via a weak link. A thermistor monitors the temperature of the absorber. The energy E deposited by a particle interaction causes a calorimetric temperature change by increasing the population of thermal phonons. The fundamental sensitivity is

$$\sigma_E^2 = \xi^2 kT[T\,C(T) + \beta E] \ , \tag{32.5}$$

where C is the heat capacity of the detector, T is the temperature of operation, k is Boltzmann's constant, and ξ is a dimensionless factor of order unity that is precisely calculable from the nature of the thermal link and the non-thermodynamic noises (*e.g.*, Johnson and/or readout noise). The first term is imposed by statistical fluctuations in the number of thermally excited phonons and on the energy in the absorber due to exchange with the thermal bath (see, *e.g.*, Ref. 49 and references therein). The second term is due to statistical fluctuations in the number of phonons excited by the absorbed radiation. The factor β is also dimensionless and $\mathcal{O}(1)$ and is also precisely calculable from the nature of the thermal link. The ratio of the second term to the first term is equal to the fractional absorber temperature change due to an energy deposition. Thus, the second term becomes appreciable when this fractional temperature change is appreciable, at which point nonlinear effects also come into play. The energy resolution typically acquires an additional energy dependence due to deviations from an ideal calorimetric model that cause position and/or energy dependence in the signal shape.

The rise time of response is limited by the internal thermal conductivity of the absorber. The decay time constant, describing the time required for the absorbed energy to flow out to the bath, is $\tau = C/G$, where G is the thermal conductance of the weak link. The above formula immediately suggests the use of crystalline dielectric absorbers and low temperatures because of the linear factor of T and because C for crystalline dielectrics drops as T^3 for T well below the material's Debye temperature (Θ_D, typically hundreds of K). Specifically, the Debye model indicates that a crystal consisting of N

atoms has

$$C = \frac{12\,\pi^4}{5}\,N\,k\left(\frac{T}{\Theta_D}\right)^3 \tag{32.6}$$

which gives $\sigma_E = 5.2\,\xi$ eV for 1 kg of germanium operated at $T = 10$ mK. (For a detector of this size the 2nd term in Eq. (32.5) is negligible.) In practice, a number of factors degrade the above result by about an order of magnitude (thermistor heat capacity and power dissipation, readout noise, *etc.*), but the predicted energy resolution for such a large mass remains attractive.

Neutron-transmutation-doped (NTD) germanium and implanted silicon semiconductors are used for thermistors. Conduction is via phonon-assisted hopping between impurity sites, yielding an exponentially decreasing resistance as a function of temperature, $R(T)$, with negative slope, dR/dT. Attachment to the absorber is usually by eutectic bonding or epoxy or by direct implantation into the absorber. Another type of temperature sensor is the superconducting phase-transition thermometers (SPT) or transition-edge sensor (TES). A SPT or TES is a superconducting film operated in the transition from superconductive to normal resistance at the transition temperature, T_c, where its resistance is a strong function of temperature with positive dR/dT. This can provide strong electrothermal negative feedback, which improves linearity, speeds up response, and mitigates variations in T_c among multiple TESs on the same absorber. $\mathrm{Nb}_x\mathrm{Si}_{1-x}$ is another thermistor material that ranges between the semiconducting and superconducting regimes as a function of the stoichiometry (defined by x). SPTs/TESs and $\mathrm{Nb}_x\mathrm{Si}_{1-x}$ thermistors are frequently deposited directly onto the absorber by sputtering or evaporation.

The readout method depends on the type of thermometer used. Doped semiconductors typically have high impedances and are well matched to low-noise JFET-based readout while SPTs/TESs are low-impedance devices requiring SQUID amplifiers.

Table 32.4: Selected experiments using sub-Kelvin detectors. The table is not exhaustive. Operation mode, detector and excitation sensor construction, baseline energy resolution, and energy resolution at a particular energy of interest E_0 are given. We quote the energy and energy resolution for "total" phonon signal, where the total phonon signal includes both recoil energy and, where relevant, drift heating. Ionization and scintillation energies are normalized so that, for electron recoils, the energy in these channels is equal to the recoil energy ("electron-equivalent" energies). For scintillation energy, this is the electron-equivalent energy deposited in the target detector, not the energy received by the photon absorber. Approximate dates of operation are also given. Key to comments: "a-Si" and "a-Ge" = amorphous silicon or germanium layers in ionization electrodes. "H-a-Si" = hydrogenated amorphous silicon. "P-implanted" = phosphorous implantation. "Interdig." = interdigitated ionization electrode design that provides some z information from ionization signal asymmetry. "Surface-event discrimination" = ability to reject events near surfaces that suffer reduced ionization yield and can be misidentified as WIMPs. "w/phonons" = using athermal phonon pulse rising edge (faster for surface events). "w/ioniz. asym." = using the asymmetry of the ionization signal on electrodes on opposite faces of interdigitated-electrode detectors. "w/phonon asym." = using the asymmetry of the phonon signal detected on opposite detector faces. "U" = not known by author. SuperCDMS energy resolutions have not been fully reported yet but are likely no worse than CDMS II.

Experiment	technique	substrate + mass	sensor	ΔE_{FWHM}[keV] at $E=0$	at E_0	E_0 [keV]	comments
WIMP dark matter							
CDMS I (1996–2000)	thermal phonon, ionization	Ge 0.16 kg	NTD Ge thermistor, H-a-Si/Al electrode	0.3 0.9	0.7 1.1	12 10.4	nuclear recoil discrimination w/ionization yield
CDMS II (2001–2008)	athermal phonon, ionization	Ge 0.25 kg	tungsten TES, a-Si/Al electrode	0.4 0.7	2.4 0.8	20.7 10.4	CDMS I+ surface-event discrimination w/phonons
SuperCDMS-SNOLAB, in development	athermal phonon, ionization	Ge 0.64 kg	tungsten TES, a-Si/Al interdig.	0.4 0.7	U U	U U	CDMS II+ surface-event discr.w/ioniz.+ phonon z asym.
EDELWEISS I (1996–2005)	thermal phonon, ionization	Ge 0.32 kg	NTD Ge thermistor, a-Si/Al a-Ge/Al	2.3 1.1	2.3 1.1	24.2 10.4	nuclear recoil discrimination w/ionization yield

Experiment	technique	substrate + mass	sensor	ΔE_{FWHM}[keV] at $E=0$	at E_0	E_0 [keV]	comments
EDELWEISS II (2006–)	thermal phonon, ionization	Ge 0.4 kg	NTD Ge thermistor, a-Si/Al interdig.	3.6 1.0	3.6 1.0	38.0 10.4	EDELWEISS I +surface-event discrimination w/ioniz.asym.
CRESST I (1996–2002)	athermal phonon	Al_2O_3 0.26 kg	tungsten SPT	0.20	0.24	1.5	no NR discr.
CRESST II (2003–)	athermal phonon, scint.	$CaWO_4$ 0.3 kg ($ZnWO_4$)	tungsten SPT (target and photon abs.)	0.3 1.0	0.3 3.5	8.1 10	NR discr. w/scint. yield
α decay							
ROSEBUD (1996–)	athermal phonon, scint.	BGO 46 g	NTD Ge thermistor (target & photon abs.)	6 U	5500 U	18 U	α discr. w/scint. yield, first det. of ^{209}Bi α decay
β decay							
Oxford ^{63}Ni (1994–1995)	athermal phonon	InSb 3.3 g	Al STJ	1.24	1.24	67	
MARE (2009–)	thermal phonon	$AgReO_4$ 0.5 mg	P-implanted Si thermistor	U	0.033	2.6	
$0\nu\beta\beta$ decay							
CUORE (2003–)	thermal phonon	TeO_2* 0.75 kg	NTD Ge thermistor	U	7	2527	

* The CUORE energy resolution is worse than can be obtained with Ge diode detectors.

32.5.2. *Athermal Phonons and Superconducting Quasiparticles* :

The advantage of thermal phonons is also a disadvantage: energy resolution degrades as $\sqrt{M}$ where M is the detector mass. This motivates the use of athermal phonons. There are three steps in the development of the phonon signal. The recoiling particle deposits energy along its track, with the majority going directly into phonons. (A minority of the energy goes directly into scintillation and ionization. Energy deposited in ionization is recovered when the carriers recombine.) The recoil and bandgap energy scales (keV and higher, and eV, respectively) are much larger than phonon energies (meV), so the full energy spectrum of phonons is populated, with phase space favoring the most energetic phonons. However, these initial energetic phonons do not propagate because of isotopic scattering (scattering due to variations in lattice ion atomic mass, rate $\propto \nu^4$ where ν is

the phonon frequency) and anharmonic decay (scattering wherein a single phonon splits into two phonons, rate $\propto \nu^5$). Anharmonic decay downshifts the phonon spectrum, which increases the phonon mean free path, so that eventually phonons can propagate the characteristic dimension of the detector. These phonons travel quasiballistically, preserve information about the position of the parent interaction, and are not affected by an increase in detector mass (modulo the concomitant larger distance to the surface where they can be sensed). Anharmonic decay continues until a thermal distribution is reached (μeV at mK temperatures), which is exhibited as a thermal increase in the temperature of the detector. If one can detect the athermal phonons at the crystal surface, keep the density of such sensors fixed as the detector surface area increases with mass, and the crystals are pure enough that the athermal phonons can propagate to the surface prior to thermalization, then an increase in detector mass need not degrade energy resolution, and can in fact improve position reconstruction. Sensors for athermal phonons are similar to those for superconducting quasiparticles described below.

Another mode is detection of superconducting quasiparticles in superconducting crystals. Energy absorption breaks superconducting Cooper pairs and yields quasiparticles, electron-like excitations that can diffuse through the material and that recombine after the quasiparticle lifetime. In crystals with very large mean free path against scattering, the diffusion length (distance traveled in a quasiparticle lifetime) is large enough (mm to cm) that the quasiparticles reach the surface and can be detected, usually in a superconducting tunnel junction (STJ) or TES/SPT.

A similar technique is applied to detect athermal phonons. Athermal phonons reaching a superconducting film on the detector surface generate quasiparticles as above. Such thin films have diffusion lengths much shorter than for superconducting crystalline substrates, only of order 100 μm to 1 mm. Thus, the superconducting film must be segmented on this length scale and have a quasiparticle sensor for each segment. The sensors may, however, be connected in series or parallel in large groups to reduce readout channel count.

The readout for athermal phonon and quasiparticle sensing depends on the type of quasiparticle detector. Tunnel junctions match well to JFET-based readouts, while TESs/SPTs use SQUID amplifiers.

32.5.3. *Ionization and Scintillation* :

While ionization and scintillation detectors usually operate at much higher temperatures, ionization and scintillation can be measured at low temperature and can be combined with a "sub-Kelvin" technique to discriminate nuclear recoils from background interactions producing electron recoils, which is critical for WIMP searches and coherent neutrino-nucleus scattering. With ionization, such techniques are based on Lindhard theory [50], which predicts substantially reduced ionization yield for nuclear recoils relative to electron recoils. For scintillation, application of Birks' law (Sec. 31.3.0) yields a similar prediction. (The reduced ionization or scintillation yield for nuclear recoils is frequently referred to as "quenching".)

Specifically, consider the example of measuring thermal phonons and ionization. All the deposited energy eventually appears in the thermal phonon channel, regardless of recoil type (modulo some loss to permanent crystal defect creation). Thus, the ionization yield—the number of charge pairs detected per unit detected energy in phonons—provides

a means to discriminate nuclear recoils from electron recoils. Similar discrimination is observed with athermal phonons and ionization and with phonons and scintillation.

In semiconducting materials of sufficient purity—germanium and silicon—electron-hole pairs created by recoiling particles can be drifted to surface electrodes by applying an electric field, similar to how this is done at $77\,K$ in high-purity germanium photon spectrometers (Sec. 31.7). There are three important differences, however, that result in the use of low fields—of order 1 V/cm—instead of the hundreds to thousands of V/cm used in 77 K detectors. First, high fields are required at 77K to deplete the active volume of thermally excited mobile carriers. At low temperature and in crystals of purity high enough to drift ionization with negligible trapping, the population of thermally excited carriers is exponentially suppressed due to the low ambient thermal energy. Second, high fields in 77K operation prevent trapping of drifting carriers on ionized impurities and crystalline defects and/or overcome space charge effects. At low temperatures, ionized impurities and space charge can be neutralized (using free charge created by photons from LEDs or radioactive sources) and remain in this state for minutes to hours. This reduces trapping exponentially and allows low-field drift. Third, a high field in a sub-Kelvin detector would result in a massive phonon signal from the drifting carriers, fully correlated with the ionization signal and thereby eliminating nuclear recoil discrimination. Readout of the charge signal is typically done with a conventional JFET-based transimpedance amplifier.

A number of materials that scintillate on their own (*i.e.*, without doping) continue to do so at low temperatures, including BaF_2, BGO, $CaWO_4$, $ZnWO_4$, $PbWO_4$, and other tungstates and molybdates. In and of itself, there is little advantage to a low-temperature scintillation measurement because detecting the scintillation is nontrivial, the quanta are large, and the detection efficiency is usually poor. Such techniques are pursued only in order to obtain nuclear-recoil discrimination. Conventional photodetectors do not operate at such low temperatures, so one typically detects the scintillation photons in an adjacent low-temperature detector that is thermally disconnected from but resides in an optically reflective cavity with the target detector.

32.6. Low-radioactivity background techniques

Written August 2009 by A. Piepke (University of Alabama).

The physics reach of low-energy rare event searches *e.g.* for dark matter, neutrino oscillations, or double beta decay is often limited by background caused by radioactivity. Depending on the chosen detector design, the separation of the physics signal from this unwanted interference can be achieved on an event-by-event basis by active event tagging, utilizing some unique event feature, or by reducing the radiation background by appropriate shielding and material selection. In both cases, the background rate is proportional to the flux of background-creating radiation. Its reduction is thus essential for realizing the full physics potential of the experiment. In this context, "low energy" may be defined as the regime of natural, anthropogenic, or cosmogenic radioactivity, all at energies up to about 10 MeV. Following the classification of [51], sources of background may be categorized into the following classes:

1. environmental radioactivity,
2. radioimpurities in detector or shielding components,
3. radon and its progeny,
4. cosmic rays,
5. neutrons from natural fission, (α, n) reactions and from cosmic-ray muon spallation and capture.

32.6.1.   *Defining the problem* : The application defines the requirements. Background goals can be as demanding as a few low-energy events per year in a ton-size detector. The strength of the physics signal to be measured can often be estimated theoretically or from limits derived by earlier experiments. The experiments are then designed for the desired signal-to-background ratio. This requires finding the right balance between clarity of measurement, ease of construction, and budget. In a practical sense, it is important to formulate background goals that are sufficient for the task at hand but doable, in a finite time. It is now standard practice to use a detector simulation to translate the background requirements into limits for the radioactivity content of various detector components, requirements for the radiation shielding, and allowable cosmic-ray flux. This strategy allows identifing the most critical components early and the allocation of analysis and development resources accordingly. The CERN code GEANT4 is a widely used tool for this task. It contains sufficient nuclear physics to allow accurate background estimations. Custom-written event generators, modeling particle correlations in complex decay schemes, are used as well.
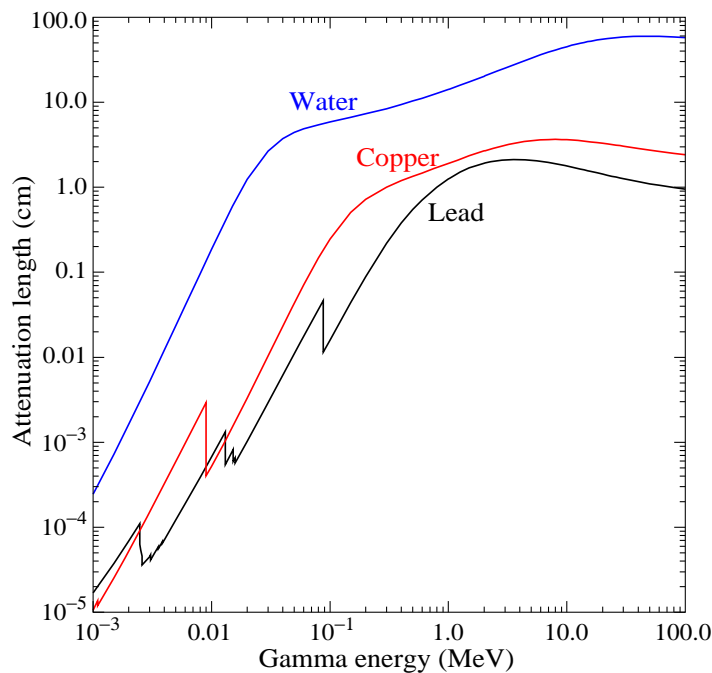

Figure 32.6: γ-ray attenuation lengths in some common shielding materials. The mass attenuation data has been taken from the NIST data base XCOM; see "Atomic Nuclear Properties" at `pdg.lbl.gov`.

32.6.2. *Environmental radioactivity* : The long-lived natural radioisotopes ^{40}K, ^{232}Th, and ^{238}U have average abundances of 2.4, 9.6 and 2.7 ppm in the earth's crust, with large local variations. In most applications, γ radiation emitted by natural radioactivity constitutes the dominant contribution to the local radiation field. Typical low-background applications require levels of natural radioactivity on the order of ppb or ppt in the detector components. Passive or active shielding is used to suppress external γ radiation down to that level. Fig. 32.6 shows the energy-dependent attenuation length $\lambda(E_\gamma)$ as a function of γ ray energy E_γ for three common shielding materials (water, copper, lead). The thickness ℓ required to reduce the external flux by a factor $f > 1$ is estimated assuming exponential damping:

$$\ell \;=\; \lambda(E_\gamma) \cdot \ln f \;. \tag{32.7}$$

At 100 keV, a typical energy scale for dark matter searches (or 2.615 MeV, for a typical double-beta decay experiment), attenuation by a factor $f = 10^5$ requires 67(269) cm of H_2O, 2.8(34) cm of Cu, or 0.18(23) cm of Pb. Such estimates allows for an order-of-magnitude estimate of the experiment dimensions. A precise estimation of the leakage of external γ radiation, including scattering and the effect of energy cuts, requires Monte Carlo simulations and determination of the radioactivity present in the laboratory. Detailed modeling of the γ flux in a large laboratory, or inside hermetic shielding, needs to cope with very small detector-hit efficiencies. It is often advantageous to calculate solid angle and mass attenuation separately. This approach reduces the computation time required for a statistically meaningful number of detector hits to manageable levels.

Because of its low density, water has relatively long attenuation lengths, resulting in rather voluminous shields. However, because water can be obtained relatively cheaply in large amounts, it has become the medium of choice for most large detectors. Water purification technology is effective and commercially available, an important consideration in view of the intrinsic radioactivity of the shield, to be discussed below. High-purity water, instrumented with photo multiplier tubes, can further serve as a Cherenkov cosmic-ray veto detector. Liquefied gases are being used for shielding as well.

32.6.3. *Radioimpurities in detector or shielding components* : After suppressing the effect of external radioactivity, radioactive impurities contained in the detector components or attached to its surfaces become important. Any material is radioactive at some level. The activity can be natural, cosmogenic, or man-made. The determination of the activity content of a specific material or component requires case-by-case analysis, and is almost never obtainable from the manufacturer. However, there are some general rules than can be used to guide the pre-selection. For detectors designed to look for electrons (for example in double-beta decay searches or neutrino detection via inverse beta decay or elastic scattering), this is the principal source of background. For devices detecting nuclear recoils (for example in dark matter searches), this is often of secondary importance as ionization signals can be actively suppressed on an event-by-event basis.

For natural radioactivity, a rule of thumb is that synthetic substances are cleaner than natural materials. Typically, more highly processed materials have lower activity content. Substances with smaller chemical reactivity tend to be cleaner. The refining process tends to remove K, Th, and U. For example, Al is often found to contain considerable amounts

of Th and U, while electrolytic Cu is very low in primordial activities. Plastics or liquid hydrocarbons, having been refined by distillation, are often quite radiopure. Tabulated radioactivity screening results for a wide range of materials can be found in Refs. 52 and 53.

The long-lived ^{238}U daughter ^{210}Pb ($T_{1/2}$=22.3 y) is found in all shielding lead, and is a background concern at low energies. This is due to the relatively high endpoint energy (Q$_\beta$=1.162 MeV) of its beta-unstable daughter ^{210}Bi. Lead parts made from selected low-U ores have specific activities of about 5–30 mBq/kg. For lower activity, ancient lead (for example from Roman ships) has been used. Because the ore processing and lead refining removed most of the ^{238}U, the ^{210}Pb decayed during the long waiting time to the level supported by the U-content of the refined lead. Lining the lead with copper to range out the low-energy radiation is another remedy. However, intermediate Z materials are an activation risk when handled above ground, as will be discussed below. ^{210}Pb is also found in solders.

The fission product ^{137}Cs can be found attached to the surface of materials. The radioactive noble gas ^{85}Kr, released into the atmosphere by nuclear reactors and nuclear fuel re-processing, is also important, especially due to its high solubility in organic materials. Post-World War II steel typically contains a few tens of mBq/kg of ^{60}Co.

Surface activity is not a material property but is added during manufacturing and handling. It can often be effectively removed by etching. Installation of low-background detectors is often done in clean rooms to avoid this contamination. Surface contamination can be quantified by means of wipe-testing with acid or alcohol wetted Whatman 41 filters. The paper filters are ashed after wiping and the residue is digested in acid. Subsequent analysis by means of mass spectroscopy or neutron activation analysis is capable of detecting less than 1 pg/cm^2 of Th and U. The most demanding low-rate experiments require screening of *all* components, which can be a time consuming task. The requirements for activity characterization depend on the experiment and the location and amount of a particular component. Monte Carlo simulations are used to quantify these requirements. Activities of the order μBq/kg or even below may need to be detected in the process. At such level of sensitivity, the characterization becomes a challenging problem in itself. Low-background α, β, and γ ray counting, mass spectroscopy, and neutron activation analysis are used.

32.6.4. *Radon and its progeny* : The noble gas ^{222}Rn, a pure α-emitter, is a ^{238}U decay product. Due to its half-life of 3.8 d it is released by surface soil and is found in the atmosphere everywhere. ^{220}Rn (^{232}Th decay product) is unimportant because of its short half-life. ^{222}Rn activity in air ranges from 10 to 100 mBq/L outdoors and 100 to thousands of mBq/L indoors. The natural radon concentration depends on the weather and shows daily and seasonal variations. Radon levels are lowest above the oceans. For electron detectors, it is not the Rn itself that creates background, but its progeny ^{214}Pb, ^{214}Bi, ^{210}Bi, which emit energetic beta and γ radiation. Thus, not only the detector itself has to be separated from contact with air, but also internal voids in the shield which contain air can be a background concern. Radon is quite soluble in water and even more so in organic solvents. For large liquid scintillation detectors, radon mobility due to convection and diffusion is a concern. To define a scale: typical double-beta-decay

searches are disturbed by a μBq (or 1/11.6 d) activity of ^{222}Rn contained in the detector medium. This corresponds to a steady-state population of 0.5 atoms in 50 μL of air (assuming 20 mBq/L of radon in the air). The criteria for leak tightness are thus quite demanding. The decay of Rn itself is a concern for some recoil type detectors, as nuclear recoil energies in α decays are substantial (76 keV in case of ^{222}Rn).

Low-activity detectors are often kept sealed from the air and continuously flushed with boil-off nitrogen, which contains only small amounts of Rn. For the most demanding applications, the nitrogen is purified by multiple distillations. Then only the Rn outgassing of the piping (due to its U internal content) determines the radon concentration. Radon diffuses readily through thin plastic barriers. If the detector is to be isolated from its environment by means of a membrane, the right choice of material is important [54].

If energies below 1 MeV are to be measured, additional care has to be taken to avoid plate-out of the long-lived radon daughter ^{210}Pb on the surfaces. This can be reduced by keeping the parts under a protective low-radon cover gas.

Radon can be detected even at the level of few atoms with solid state, scintillation, or gas detectors by exploiting the fast decay sequences of ^{214}Bi and ^{214}Po. The efficiency of these devices is sometimes boosted by electrostatic collection of charged radon into a small detector.

32.6.5.   *Cosmic rays* : Cosmic radiation, discussed in detail in Chapter 26, is a source of background for just about any non-accelerator experiment. Primary cosmic rays are about 90% protons, 9% alpha particles, and the rest heavier nuclei (Fig. 26.1). They are totally attenuated within the first the first few hg/cm^2 of atmospheric thickness. At sea level secondary particles ($\pi^\pm : p : e^\pm : n : \mu^\pm$) are observed with relative intensities (1 : 13 : 340 : 480 : 1420) for $E < 1\,\text{GeV}$ (Ref. 55; also see Fig. 26.3).

All but the muon and the neutron components are readily absorbed by overburden such as building ceilings and passive shielding. Only if there is very little overburden (less than a few $\times$ 10 g cm^{-2} in rock) do pions and protons need to be considered when estimating the production rate of cosmogenic radioactivity.

Sensitive experiments are thus operated deep underground where essentially only muons penetrate. As shown in Fig. 26.6, the muon intensity falls off rapidly with depth. Active detection systems capable of tagging events correlated in time with cosmic-ray activity are needed, depending on the overburden. Such experiments are described in Sec. 32.3.1.

The muonic background is only related to low-radioactivity techniques insofar as photonuclear interactions of muons can produce long-lived radioactivity. This happens at any depth, and it constitutes an essentially irreducible background.

Cosmogenic activation of components brought from the surface is also an issue. Proper management of parts and materials above ground during machining and detector assembly minimizes the accumulation of long-lived activity. Cosmogenic activation is most important for intermediate Z materials such as Cu and Fe. For the most demanding applications, metals are stored and transported under sufficient shielding to stop the hadronic component of the cosmic rays. Parts, *e.g.*, the nickel tubes for the ^{3}He counters in SNO, can be stored underground for long periods before being used. Underground machine shops are also sometimes used to limit the duration of exposure at the surface.

32.6.6.   *Neutrons* : Neutrons contribute to the background of low-energy experiments in different ways: directly through nuclear recoil in the detector medium, and indirectly, through the production of radio nuclides inside the detector and its components. The latter mechanism allows even remote materials to contribute to the background by means of penetrating γ radiation, since inelastic scattering of fast neutrons or radiative capture of slow neutrons can result in the emission of γ radiation. Neutrons are thus an important source of low-energy background. They are produced in different ways:

1. At the earth's surface neutrons are the most frequent cosmic-ray secondaries other than muons;
2. Energetic tertiary neutrons are produced by cosmic-ray muons in nuclear spallation reactions with the detector and laboratory walls;
3. In high Z materials, often used in radiation shields, nuclear capture of negative muons results in emission of neutrons;
4. Natural radioactivity has a neutron component through spontaneous fission and (α, n)-reactions.

A calculation with the hadronic simulation code FLUKA, using the known energy distribution of secondary neutrons at the earth's surface [56], yields a mass attenuation of 1.5 hg/cm^2 in concrete for secondary neutrons. If energy-dependent neutron-capture cross sections are known, then such calculations can be used to obtain the production rate of radio nuclides.

At an overburden of only few meters, water equivalent neutron production by muons becomes the dominant mechanism. Neutron production rates are high in high-Z shielding materials. A high-Z radiation shield, discussed earlier as being effective in reducing background due to external radioactivity, thus acts as a source for cosmogenic tertiary high-energy neutrons. Depending on the overburden and the radioactivity content of the laboratory, there is an optimal shielding thickness. Water shields, although bulky, are an attractive alternative due to their low neutron production yield and self-shielding.

Neutron shields made from plastic or water are commonly used to reduce the neutron flux. The shield is sometimes doped with a substance having a high thermal neutron capture cross section (such as boron) to absorb thermal neutrons more quickly. The hydrogen serves as a target for elastic scattering, and is effective in reducing the neutron energy. Neutrons from natural radioactivity have relatively low energies and can be effectively suppressed by a neutron shield. Such a neutron shield should be inside the lead to be effective for tertiary neutrons. However, this is rarely done as it increases the neutron production target (in form of the passive shield), and costs increase as the cube of the dimensions. An active cosmic-ray veto is an effective solution, correlating a neutron with its parent muon. This solution works best if the veto system is as far removed from the detector as feasible (outside the radiation shield) to correlate as many background-producing muons with neutrons as possible. The vetoed time after a muon hit needs to be sufficiently long to assure neutron thermalization. The average thermalization and capture time in lead is about 900 μs [51].   The veto-induced deadtime, and hence muon hit rate on the veto detector, is the limiting factor for the physical size of the veto system (besides the cost). The background caused by neutron-induced radioactivity with live times exceeding the veto time cannot be addressed in this way. Moving the detector

deep underground, and thus reducing the muon flux, is the only technique addressing all sources of neutron background.

References:
1. R.M. Baltrusaitis *et al.*, Nucl. Instrum. Methods **A20**, 410 (1985).
2. T. Abu-Zayyad *et al.*, Nucl. Instrum. Methods **A450**, 253 (2000).
3. T. Nonaka *et al.*, Nucl. Phys. B Proc. Suppl. **190** , 26, (2009).
4. J. Abraham *et al.*, [Pierre Auger Collab.], Nucl. Instrum. Methods **A620**, 227 (2010).
5. Y. Takahashi and the JEM-EUSO Collab., New J. Phys. **11**, 065009 (2009).
6. F. Arqueros, J. Hrandel, and B. Keilhauer, Nucl. Instrum. Methods **A597**, 23 (2008).
7. F. Arqueros, J. Hrandel, and B. Keilhauer, Nucl. Instrum. Methods **A597**, 1 (2008).
8. J. Boyer *et al.*, Nucl. Instrum. Methods **A482**, 457 (2002);
   M. Kleifges for the Pierre Auger Collab., Nucl. Instrum. Methods **A518**, 180 (2004).
9. M. Ave *et al.*, [AIRFLY Collab.], Astropart. Phys. **28**, 41 (2007).
10. J.T. Brack *et al.*, Astropart. Phys. **20**, 653, (2004).
11. B. Fick *et al.*, JINST **1**, 11003, (2006).
12. J. Abraham *et al.*, [Pierre Auger Collab.], Astropart. Phys. **33**, 108 (2010).
13. J. Abraham *et al.*, [Pierre Auger Collab.], Astropart. Phys. **34**, 368 (2011).
14. M. Unger *et al.*, Nucl. Instrum. Methods **A588**, 433 (2008).
15. T.K. Gaisser and A.M. Hillas, *Proc. 15th Int. Cosmic Ray Conf.* (Plovdiv, Bulgaria, 13–26 Aug. 1977).
16. J. Holder *et al.*, *Proc. 4th International Meeting on High Energy Gamma-Ray Astron.*, eds. F.A. Aharonian, W. Hofmann, and F. Rieger, AIP Conf. Proc. **1085**, 657 (2008).
17. J.A. Hinton, New Astron. Rev. **48**, 331 (2004).
18. J. Albert *et al.*, Astrophys. J. **674**, 1037 (2008).
19. Lectures given at the International Heraeus Summer School, "Physics with Cosmic Accelerators," Bad Honnef, Germany, July 5–16 (2004), `astro-ph/0508253`.
20. T.C. Weekes *et al.*, Astrophys. J. **342**, 379 (1989).
21. A.M. Hillas *et al.*, Astrophys. J. **503**, 744 (1998).
22. F.A. Aharonian, *et al.*, Astrophys. J. **636**, 777 (2006).
23. L.A. Bernstein *et al.*, "Report on the Depth Requirements for a Massive Detector at Homestake" (2009); `arXiv:0907.4183`.
24. Y. Ashie *et al.*, Phys. Rev. **D71**, 112005 (2005).
25. S. Kasuga *et al.*, Phys. Lett. **B374**, 238 (1996).
26. M. Shiozawa, Nucl. Instrum. Methods **A433**, 240 (1999).
27. J. Hosaka *et al.*, Phys. Rev. **D73**, 112001 (2006).
28. J. Boger *et al.*, Nucl. Instrum. Methods **A449**, 172 (2000).
29. K. Griesen, Phys. Rev. Lett. **16**, 748 (1966); G.T. Zatsepin and V.A. Kuzmin, JETP Lett. **4**, 78 (1966).
30. G.A. Askaryan, JETP **14** 441 (1962); G.A. Askaryan JETP **21**, 658 (1965).

31.   D. Saltzberg *et al.*, Phys. Rev. Lett. **86**, 2802 (2001); O. Scholten et al., J. Phys. Conf. Ser. **81**, 012004 (2007).

32.   S.R. Klein, `arXiv:1012.1407`.

33.   R.D. Dagkesamanskii and I.M. Zheleznykh, Sov. Phys. JETP Lett. **50**, 233 (1989).

34.   P. Gorham *et al.*, Phys. Rev. Lett. **103** 051103 (2009). The published limit is corrected in an erratum, P. Gorham *et al.*, `arXiv:1011.5004`.

35.   P. Allison *et al.*, `arXiv:1105.2854`; P. Allison *et al.*, Nucl. Instrum. & Meth. **A604**, S64 (2009); the ARA Collaboration, presented at the *2011 Intl. Cosmic Ray Conf.*

36.   L. Gerhardt *et al.*, Nucl. Instrum. Methods **A624**, 85-91 (2010); S. Barwick, preprint `arXiv:astro-ph/0610631`; T. Barella, S. Barwick, and D. Saltzberg, J. Glaciology **57**, 61 (2011).

37.   S. Hoover *et al.*, Phys. Rev. Lett. **105**, 151101 (2010).

38.   I. Kravchenko *et al.*, Phys. Rev. **D73**, 082002 (2006); I. Kravchenko *et al.*, Astropart. Phys. **19**, 15 (2003).

39.   M. Schaumann, "The XENON 100 Dark Matter Experiment," *10th Conf. on the Intersections of Part. & Nucl. Phys.*, (2009), to be published in AIP Conf. Proc.

40.   A. Bolotnikov and B. Ramsey, Nucl. Instrum. Methods **A496**, 360 (1997).

41.   E. Aprile *et al.*, Phys. Rev. **B76**, 014115 (2007).

42.   C.M.B. Monteiro *et al.*, "Secondary scintillation yield in pure xenon," JINST 2 P05001 (2007), doi 10.1088/1748-0221/2/05/P05001.

43.   W.H. Lippincott *et al.*, Phys. Rev. **C78**, 035801 (2008).

44.   W. Blum and L. Rolandi, *Particle Detection with Drift Chambers,* Springer-Verlag (1994).

45.   R.S. Chandrasekharan, "Noble Gas Scintillation-Based Radiation Portal Monitor and Active Interrogation Systems," IEEE Nucl. Sci. Symposium Conference Record (2006).

46.   C.J. Martoff *et al.*, Nucl. Instrum. Methods **A440**, 355 (2000).

47.   *Cryogenic Particle Detection*, ed. by C. Enss, (Springer-Verlag: Berlin, 2005).

48.   *Proc. 13th Inter. Workshop on Low Temperature Detectors*, AIP Conference Proc. (2009); see also *Proceedings* of previous occurrences of this workshop.

49.   S.H. Moseley, J.C. Mather, and D. McCammon, J. Appl. Phys. **56**, 1257 (1984).

50.   J. Lindhard *et al.*, Mat. Fys. Medd. K. Dan. Vidensk. Selsk. **33**, 10 (1963).

51.   G. Heusser, Ann. Rev. Nucl. and Part. Sci. **45**, 543 (1995).

52.   P. Jagam and J.J. Simpson, Nucl. Instrum. Methods **A324**, 389 (1993).

53.   D.S. Leonard *et al.*, Nucl. Instrum. Methods **A591**, 490 (2008).

54.   M. Wojcik *et al.*, Nucl. Instrum. Methods **A449**, 158 (2000).

55.   National Council on Radiation Protection and Measurement, Report 94, Bethesda, MD (1987).

56.   M.S. Gordon *et al.*, IEEE Trans. **NS51**, 3427 (2004).